RESEARCH ARTICLE
SPACE PHYSICS: MAGNETOSPHERIC PHYSICS

Earth and Planetary Physics
8: 119–132, 2024
doi: 10.26464/epp2023068

Two methods for separating the magnetospheric solar wind charge exchange soft X-ray emission from the diffuse X-ray background

YingJie Zhang[1,2], TianRan Sun[1*], Jennifer. A. Carter[3], WenHao Liu[4], Steve Sembay[3], ShuiNai Zhang[4], Li Ji[4], and Chi Wang[1,2*]

[1]State Key Laboratory of Space Weather, National Space Science Center, Chinese Academy of Sciences, Beijing 100190, China;

[2]College of Earth and Planetary Sciences, The University of Chinese Academy of Sciences, Beijing 100190, China;

[3]School of Physics and Astronomy, The University of Leicester, Leicester, UK;

[4]Purple Mountain Observatory, Chinese Academy of Sciences, Nanjing 210008, China

Key Points:

- Spectral compositions obtained by two methods are very similar, and the changesin intensity over time are highly consistent.
- Difference between two methods is due to the fitted diffuse X-ray background, which is most significant when energy is less than 0.7 keV.
- Difference between two methods is not related to the solar wind conditions.

Citation: Zhang, Y. J., Sun, T. R., Carter, J. A., Liu, W. H., Sembay, S., Zhang, S. N., Ji, L., and Wang, C. (2024). Two methods for separating the magnetospheric solar wind charge exchange soft X-ray emission from the diffuse X-ray background. *Earth Planet. Phys.*, *8*(1), 119–132. http://doi.org/10.26464/epp2023068

Abstract: Solar wind charge exchange (SWCX) is the process of solar wind high-valence ions exchanging charges with neutral components and generating soft X-rays. Recently, detecting the SWCX emission from the magnetosphere is proposed as a new technique to study the magnetosphere using panoramic soft X-ray imaging. To better prepare for the data analysis of upcoming magnetospheric soft X-ray imaging missions, this paper compares the magnetospheric SWCX emission obtained by two methods in an XMM-Newton observation, during which the solar wind changed dramatically. The two methods differ in the data used to fit the diffuse X-ray background (DXB) parameters in spectral analysis. The method adding data from the ROSAT All-Sky Survey (RASS) is called the RASS method. The method using the quiet observation data is called the Quiet method, where quiet observations usually refer to observations made by the same satellite with the same target but under weaker solar wind conditions. Results show that the spectral compositions of magnetospheric SWCX emission obtained by the two methods are very similar, and the changes in intensity over time are highly consistent, although the intensity obtained by the RASS method is about 2.68 ± 0.56 keV cm^{-2}s^{-1}sr^{-1} higher than that obtained by the Quiet method. Since the DXB intensity obtained by the RASS method is about 2.84 ± 0.74 keV cm^{-2}s^{-1}sr^{-1} lower than that obtained by the Quiet method, and the linear correlation coefficient between the difference of SWCX and DXB obtained by the two methods in different energy band is close to −1, the differences in magnetospheric SWCX can be fully attributed to the differences in the fitted DXB. The difference between the two methods is most significant when the energy is less than 0.7 keV, which is also the main energy band of SWCX emission. In addition, the difference between the two methods is not related to the SWCX intensity and, to some extent, to solar wind conditions, because SWCX intensity typically varies with the solar wind. In summary, both methods are robust and reliable, and should be considered based on the best available options.

Keywords: solar wind charge exchange (SWCX); ROSAT All-Sky Survey (RASS); soft X-ray; X-ray imaging; magnetosphere

1. Introduction

The ROSAT observation of Comet C/Hyakutake 1996 B2 (Lisse et al., 1996) led to the discovery of soft X-rays generated by solar wind charge exchange (SWCX) (Cravens, 1997). SWCX occurs when highly charged ions in the solar wind interact with neutral atoms or molecules. The ions acquire an electron and enter the excited state, then return to the ground state by emitting soft X-ray photons.

With the launch of more X-ray satellites, SWCX emission from the Earth (Wargelin et al., 2004), Jupiter (Branduardi-Raymont et al., 2004), Mars (Dennerl et al., 2006), Venus (Dennerl, 2008), the moon (Collier et al., 2014) and the heliosphere (Galeazzi et al., 2014) has been widely observed (Bhardwaj et al., 2007; Sibeck et al., 2018). SWCX emission in Earth's space is not only an important background for astronomical research (Kuntz, 2019), but also includes information on the position of the magnetopause and the boundary of the cusp regions. Therefore, a new method for

---

First author: Y. J. Yang, yjzhang@spaceweather.ac.cn
Correspondence to: T. R. Sun, trsun@swl.ac.cn
C. Wang, cw@swl.ac.cn
Received 19 FEB 2023; Accepted 27 SEP 2023.

studying the magnetosphere using soft X-ray panoramic imaging has been proposed and rapidly developed (Branduardi-Raymont et al., 2012; Collier et al., 2012; Walsh et al., 2016; Sibeck et al., 2018). Based on this, the Solar Wind Magnetospheric Ionosphere Link Explorer (SMILE) with a unique large field of view (FOV; 16° × 27°), the European Space Agency (ESA) and Chinese Academy of Sciences (CAS) Joint Soft X-ray Imager, will be launched in 2025 (Branduardi-Raymont et al., 2018; Wang C and Branduardi-Raymont, 2020).

The spectrum of SWCX is characterized by emission lines from highly ionized ions in the solar wind such as C^{5+}, N^{6+}, O^{6+}, and O^{7+}, with no continuum components (Koutroumpa et al., 2009a). Since the magnetospheric SWCX emission is smooth across the FOV of all X-ray instruments, and it does not have sufficiently unique spectral features compared with the diffuse X-ray background (DXB) composed of the cosmic diffuse X-ray background (CDXB) and the heliospheric SWCX emission, it is challenging to unambiguously separate it from the DXB.

ROSAT All-Sky Survey (RASS) provides the best CDXB maps for studying the diffuse emission at energies below 2 keV (Snowden et al., 1997). The CDXB observed in the 1/4 keV band (R12: 0.12–0.284 keV) is mainly originated from the Local Hot Bubble (LHB), and the Galactic Halo (GH) with a significant contribution at high latitudes (McCammon and Sanders, 1990; Kuntz and Snowden, 2000). The CDXB observed in the 3/4 keV band (R45: 0.47–1.21 keV) is mainly originated from the Galactic disk and halo, and the active galactic nuclei (AGNs) with a 30–50% contribution at intermediate and high latitudes (Snowden et al., 1997). The CDXB observed in the R67 (0.76–2.04 keV) band above 1 keV is almost all originated from the AGNs (Mushotzky et al., 2000). There was a time-variable signal in the 1/4 keV and 3/4 keV bands, called the long-term enhancements (LTEs) (Snowden et al., 1994, 1995), which was later recognized to be caused by the charge exchange between the solar wind and geocoronal neutral hydrogen (Cox, 1998; Cravens et al., 2001). Since the magnetospheric SWCX (the LTEs) was removed from the RASS (Snowden et al., 1995; Kuntz et al., 2015), and the heliospheric SWCX emission accounts for about 27% of the observed flux in the R12 band and 6% in the R45 band (Uprety et al., 2016), it is widely accepted that the RASS is composed of many spectrally and spatially highly variable but relatively temporally stable CDXB components.

The heliospheric SWCX emission is generated by the interaction between the solar wind ions and the neutral interstellar medium entering the solar system (Cox, 1998). It has long-time-scale variations related to the solar cycle (Qu Z et al., 2022), because short-time-scale variations from solar wind tend to be offset by integration along the line-of-sight (LOS) and emission region size (Cravens et al., 2001). In addition, it strongly depends on the observation geometry, as its emission level can significantly change when the LOS is parallel to the solar wind Parker spiral shock front, especially when it passes through the Helium focusing cone (Koutroumpa et al., 2006, 2007, 2009b; Galeazzi et al., 2012). It is worth noting that thoroughly distinguishing the diffuse X-rays emitted by the heliosphere and LHB (one of the CDXB components) is very challenging, which has sparked controversy in astrophysics about the existence of LHB (Lallement, 2004b; Koutroumpa et al., 2009c; Robertson et al., 2009; Galeazzi et al., 2014; Snowden et al., 2014).

There are two main methods for separating the magnetospheric SWCX emission from the DXB. The two methods differ in the data used to fit the DXB parameters in spectral analysis. The method adding data from RASS is called the RASS method (Snowden et al., 2004; Kuntz and Snowden, 2008a; Henley and Shelton, 2008; Koutroumpa et al., 2009b; Slavin et al., 2013; Zhang YJ et al., 2022). The method using the quiet observation is called the Quiet method. The quiet observation usually refers to the observation from the same satellite with the same target and under weaker solar wind conditions, but sometimes it can also be a part of the scientific observation at the expense of this part of scientific data (Fujimoto et al., 2007; Carter and Sembay, 2008; Ezoe et al., 2010, 2011; Carter et al., 2010, 2011; Carter et al., 2012; Ishikawa et al., 2013; Wargelin et al., 2014; Ishi et al., 2019; Asakura et al., 2021). The method of extracting magnetospheric SWCX emission is of great significance for upcoming magnetospheric soft X-ray imaging missions such as SMILE. However, the reliability and differences between the two methods have not yet been reported.

This paper compares the magnetospheric SWCX emission obtained by the two methods in an XMM-Newton observation, during which the solar wind changed dramatically. Section 2 displays the data. Section 3 describes the data analysis. Section 4 shows the results. Sections 5 and 6 provide discussions and conclusions, respectively.

2. Data

XMM-Newton original data files are available on the XMM-Newton science archive[1]. The scientific observation used to study the magnetospheric SWCX emission occurred on February 2, 2016. Its observation target is M13 (16 h 41 m 43.76 s, +36d 27' 57.6", J2000), and its observation ID is 0760750101. There is an observation with the same target of M13 occurred on January 28, 2002, with the observation ID 0085280301. Table 1 provides detailed information on these two observations. Henceforth, they are referred to as the Obs2958 and Obs391, respectively.

Figure 1 shows the solar wind conditions and the LOS of Obs2958 and Obs391. Firstly, Obs391 can be used as the quiet observation of Obs2958, because the solar wind conditions of Obs391 are significantly weaker than that of Obs2958. As shown in panels (a–d), the average solar wind proton density, velocity, flux and the ratio of O^{7+} to O^{6+} which characterizing the ionization state of ions for Obs2958 are 18.0 n/cc, 333.9 km/s, 5622.6 km·n/s/cc and 0.48, while that for Obs391 are 3.6 n/cc, 375.8 km/s, 1357.7 km·n/s/cc and 0.12, respectively. Secondly, the LOS of Obs391 meets the stricter condition for quiet observations. As shown in panels (e2–f2), the LOS of Obs391 is on the night side of the magnetosphere, where the magnetospheric SWCX emission is very weak. Thirdly, the influence of heliospheric SWCX emission on quiet observation data and RASS data is similar, as the observation time of Obs391 is at the solar maximum (2002), similar to that of RASS data (1990–1991). In summary, quiet observation itself is very rare, and meeting the three more stringent conditions mentioned above is extremely rare. The observation with observation ID 0085280801 also meets the above three conditions, but its

---

[1] http://nxsa.esac.esa.int/nxsa-web/

Table 1. Two XMM-Newton observations of target M13.

Obs.ID	Revolution	Instruments	Start time	End time	Exposure (h)
0760750101	2958	MOS1	2016/2/2 11:56	2016/2/3 16:11	28.24
		MOS2	2016/2/2 11:57	2016/2/3 16:11	28.23
		pn	2016/2/2 12:19	2016/2/3 16:07	27.79
0085280301	391	MOS1	2002/1/28 1:59	2002/1/28 7:02	5.06
		MOS2	2002/1/28 1:59	2002/1/28 7:02	5.06
		pn	2002/1/28 1:59	2002/1/28 7:02	4.43

Note. All three X-ray cameras (MOS1, MOS2 and pn) are in full-frame mode and with the medium filter.

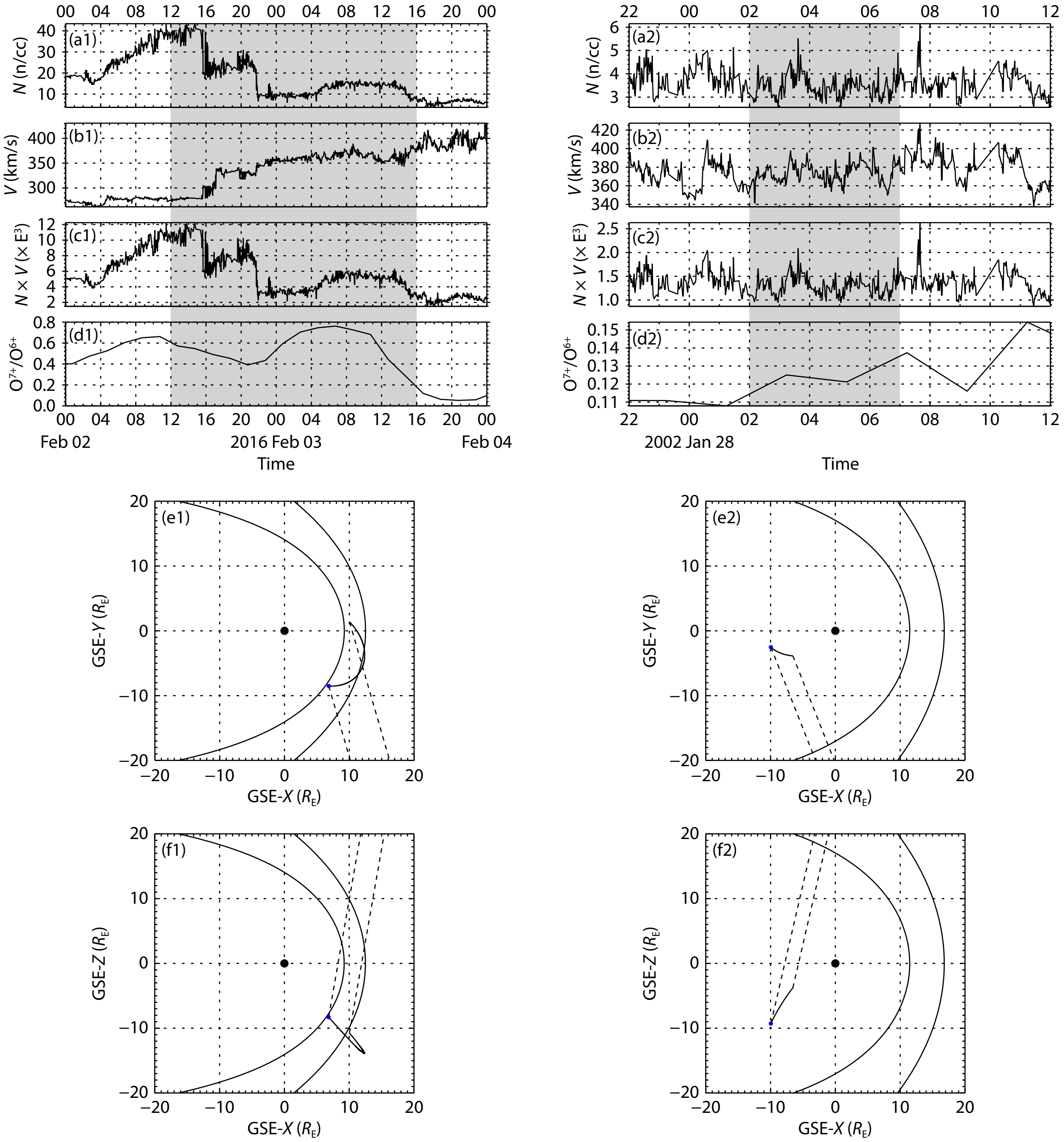

Figure 1. The solar wind conditions and LOS of Obs2958 (left) and Obs391 (right). Solar wind conditions: (a) proton density, (b) velocity, (c) proton flux and (d) the ratio of O^{7+} to O^{6+}. Panels (e–f) shows the LOS in the Geocentric Solar Ecliptic (GSE) coordinates, where the location of magnetopause (Shue et al., 1997) and bow shock (Chao J et al., 2002) are calculated using the average solar wind conditions. The curved line with a blue dot (start time) is the orbital position of XMM-Newton, while the dashed line extending from it represents the observation direction.

data is too poor. In fact, the data of Obs391 is also poor, but fortunately the fitting is adequate, which will be displayed in the following text.

For Obs2958, firstly, the solar wind conditions have very significant changes, which is conducive to studying the influence of different solar wind conditions. As shown in panels (a1–c1), the variation range of solar wind proton density, velocity and flux for Obs2958 are 3.7–43.4 n/cc, 261.9–430.6 km/s and 1490.2–12240.3 km·n/s/cc, respectively. Secondly, as shown in panels (e1–f1), the LOS of Obs2958 is near the subsolar magnetopause where the SWCX emission is very strong, and it is very similar to the future LOS of SMILE. In addition, the LOS of Obs2958 and Obs391 do not pass through the helium focusing cone or, to first order, parallel to the Parker spiral, so their heliospheric SWCX emissions should not be very strong and varied, which is conducive to studying the magnetospheric SWCX emission.

RASS data is provided by the HEASARC X-ray Background Tool[2]. We used this tool to extract the spectrum in a circular region with a radius of 1° centered on the same target M13. This tool also provided an appropriate redistribution matrix file (RMF) and the average galactic HI column density of 1.39×10^{20} atoms/cm^2.

3. Data Analysis

3.1 Data Reduction

We used the Science Analysis System (SAS) software (version 20.0.0)[3] and the Current Calibration Files (CCFs) released on 2023 April 5, to analyze the XMM-Newton data. First, we ran the SAS task emproc for MOS cameras and epproc for the pn camera, to produce calibrated event lists. Second, we used the standard filtering expressions to select X-ray event lists: (*PATTERN* <= 12) && (*#XMMEA_EM*) for MOS cameras and (*PATTERN* == 0) && (*FLAG* == 0) for the pn camera. The PATTERN filter selected events from the entire X-ray pattern library for MOS cameras, but only single pixel events for the pn camera, which optimized the energy resolution of pn camera below 2 keV. The *#XMMEA_EM* filter for MOS cameras removed events from regions of known bright pixels or columns or close to the CCD boundaries. The *FLAG* == 0 for pn camera not only removed the residual noisy pixels, but also masked events from adjacent regions to noisy pixels. Third, some individual CCDs in the MOS detectors sometimes operate in an abnormal state, resulting in strong enhancement of background below 1 keV (Kuntz and Snowden, 2008b). Therefore, we used the SAS task emanom to check and exclude the CCD5 of MOS2 in Obs2958.

3.2 Soft Proton Flares

Soft protons can produce spectrally smooth, broad-band, full-FOV signals, which can even be many times stronger in intensity to SWCX emission. Soft proton contamination has different temporal behaviors: highly variable, slowly varying, fairly or nearly flat, or a combination of temporal behaviors. The highly variable signals, also known as soft proton flares, manifest as a sudden increase in the count rate and affects a large number of XMM-Newton observations (Kuntz and Snowden, 2008b; Walsh et al., 2014). To remove soft proton flares, we used the SAS task espfilt which fitted a roughly Gaussian to the histogram of count rates and created the good time intervals (GTIs) filter for those times where the count rate was within 3.0 sigma (Obs2958) and 1.5 sigma (Obs391) of the Gaussian peak's count rate. Figure 2 shows the GTIs of Obs2958, and Figure S1 shows the temporal filtering results of Obs391. It can be seen that soft proton flares of Obs391 are very strong, especially for the pn camera, even low count rate exposure of about 5000 seconds may still be contaminated by residual soft protons.

3.3 Astronomical Point Sources

Astronomical point sources are highly spectrally and spatially variable, and some of them are comparable or stronger in intensity to SWCX emission. To remove astronomical point sources, we used the source lists available in the XMM-Newton archive to create a region filter that removed events within a 35 arcsec radius (about 90% of the on-axis point spread function) center on each point source. Then, we manually checked the remaining image and used larger removal radius for those wider point sources. For Obs2958 and Obs391, we have used the same region filter. In addition, we only extracted events within a radius of 11.7 arcmin centered on the common sky location (16:41:40.7, +36:27:36.9, J2000). Figure 3 shows the data extraction region of Obs2958, including 192 astronomical point sources to be removed.

3.4 Particle Background

The particle background is produced by cosmic rays directly penetrating the CCD or indirectly by the fluorescence of satellite material to which the detector is exposed. It has a relatively stable spectrum and intensity, and can be well estimated using the data obtained when the instruments are in the filter wheel closed (FWC) configuration (not open to the sky). Since the FWC data also contains the electronic readout noise, it can also be removed at the same time. To remove the particle background, we used the SAS task evqpb with the default parameters to acquire the background event lists, and then extracted the data using the same extraction expressions as the observation. Next, we derived the rescaling factor by comparing the background spectrum to the observation spectrum in the energy of 2.5–12.0 keV for MOS cameras, and the same energy band excluding 7.2–10 keV for the pn camera, where the contributions from other background were negligible. Finally, the rescaling factors of Obs2958 were 1.198 (MOS1), 1.025 (MOS2) and 1.164 (pn), and that of Obs391 were 1.836 (MOS1), 1.477 (MOS2) and 1.391 (pn), respectively.

3.5 Spectral Model

After the previous steps, we obtained a clean spectrum consisting of the target magnetospheric SWCX emission and four backgrounds: residual instrument lines, residual soft proton contamination (RSP) and the DXB composed of CDXB and heliospheric SWCX emission. The residual instrument lines of Al K_α and Si K_α can be modeled by two zero-width Gaussian models with energy fixed at 1.49 keV and 1.75 keV for MOS cameras, and a zero-width

---

[2] https://heasarc.gsfc.nasa.gov/cgi-bin/Tools/xraybg/xraybg.pl

[3] https://www.cosmos.esa.int/web/xmm-newton/sas-download/

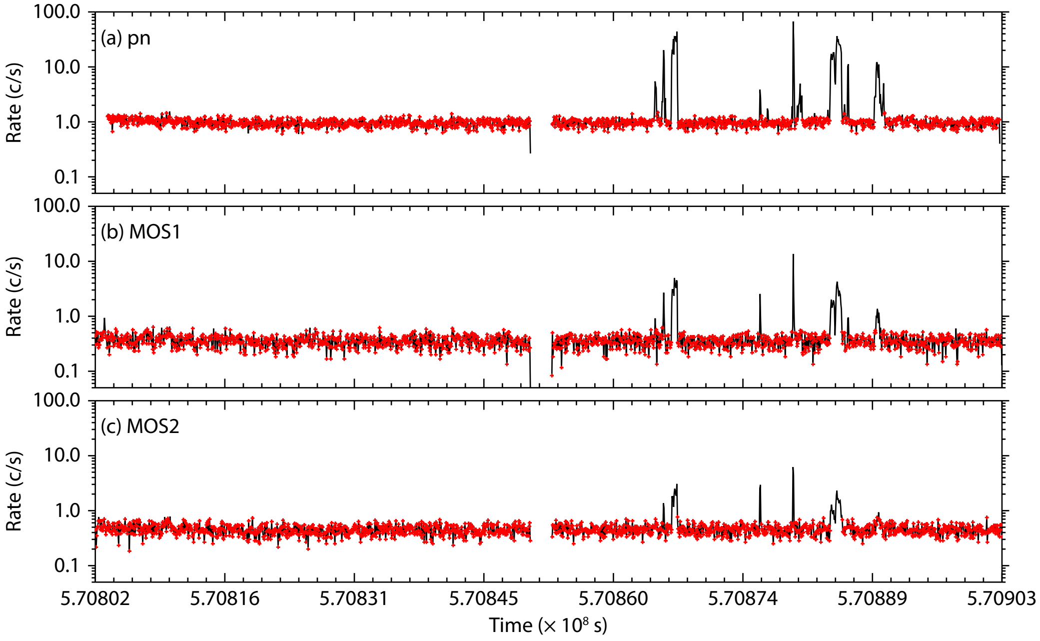

Figure 2. Count rate curve of each camera for Obs2958 in the 2.5–8.5 keV band, where the red represents the GTIs. The time is in the XMM-Newton time system, which is the number of seconds since the start of 1999.

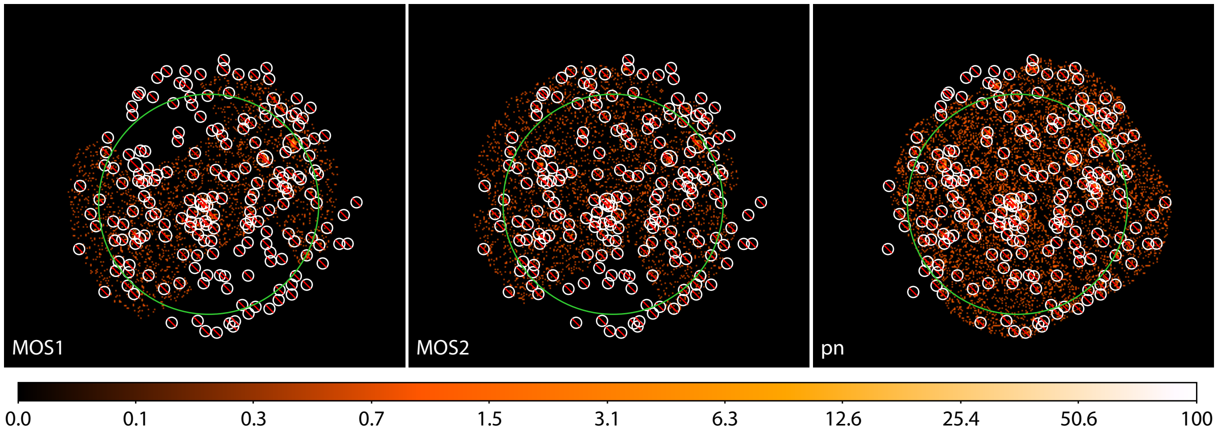

Figure 3. Image of each camera for Obs2958 in the 0.3–2.0 keV band. The small white circle with a red slash shows the astronomical point source to be removed. The large green circle shows the data extraction region.

Gaussian model with energy fixed at 1.49 keV for the pn camera. The temporal variation of the RSP, by construction, is not strong, and the RSP can be modeled by a power law which is not folded through the instrumental effective areas (Kuntz and Snowden, 2008a). Because it is different in different cameras, each camera is assigned a power law model with a separate diagonal response matrix. The DXB can usually be modeled by a three-component model (Kuntz and Snowden, 2008a): (1) a cold ($E \sim 0.1$ keV), unabsorbed thermal plasma component, representing emission from the LHB or heliosphere; (2) a hot ($E \sim 0.25$–0.7 keV), absorbed thermal plasma component, representing emission from the GH; (3) an absorption power law with index ~1.46, representing the unresolved cosmic background. The APEC (Smith et al., 2001) model with the redshift parameter fixed at zero is used to model the plasma components. The element abundances are set by the wilm table (Wilms et al., 2000). The tbabs model with the galactic HI column density fixed at 1.39×10^{20} atoms/cm^2 is used to model the absorption. SWCX emission can be modeled by a series of zero-width Gaussian models with energies fixed at likely transitions from solar wind ions (Carter et al., 2010). For the emission lines of CV, CVI, NVI, NVII, OVII and OVIII, the theoretical collision cross-sections (Bodewits et al., 2007) with a speed of 400 km/s (closest to the average speed of Obs2958) were used. In order to obtain the time-varying SWCX emission, as shown in panel (b1) of Figure 1, the theoretical collision cross-sections with a speed of 200 km/s were used before 17:00 on February 2nd, and that with a speed of 400 km/s were used thereafter. The normalization of dominant transition for each ion is free, while the normalizations of other weak transitions are linked to the dominant transition by the ratios of collision cross-section. At higher energies, other likely transitions from heavier solar wind ions (Ne, Mg, Fe, etc.) are added empirically. Furthermore, the relative normalization between the three cameras can be characterized by a constant model, where the normalization of pn camera is fixed to 1.0 in this paper.

3.6 Spectral Analysis of RASS Method and Quiet Method

We used the X-Ray Spectral Fitting Package (XSPEC) in HEASoft (version 6.29)[4] to analyze the spectrum. The two methods differ in the data used to fit the DXB parameters in spectral analysis. RASS method adds a RASS spectrum to constrain DXB parameters (Kuntz and Snowden, 2008a). We fitted the four-component model (including residual instrument lines, RSP, DXB and SWCX emission) to the comprehensive spectrum composed of three spectra of three cameras (Obs2958) and one RASS spectrum. For the RASS spectrum, only the DXB model was applied. Quiet method directly fits the spectrum of quiet observation to obtain the best-fitting DXB parameters (Carter et al., 2010). The Quiet method is divided into two steps, and the fitted energy bands used in both steps are 0.3–6.5 keV, which is the same as the RASS method. First, we fitted the three-component model (except for SWCX emission) to the comprehensive spectrum composed of three spectra of three cameras (Obs391) to acquire the best-fitting DXB parameters. Table 2 lists the best-fitting parameters for Obs391, and Figure 4 shows the clean spectrum and best-fitting models. It demonstrates that the fitting of Obs391 is adequate, although the RSP is very strong and even comparable in intensity to DXB emission. Secondly, we fitted the four-component model to the comprehensive spectrum composed of three spectra of three cameras (Obs2958), where the DXB parameters were fixed to the best-fitting DXB parameters obtained from Obs391.

4. Results

4.1 DXB and Magnetospheric SWCX Obtained by Two Methods

Table 3 lists the best-fitting parameters of RSP and DXB for Obs2958 obtained by the two methods, and Figure 5 shows the clean spectrum and best-fitting models. First, the temperature and normalization of LHB emission obtained by the two methods

Table 2. Best-fitting parameters for Obs391.

Conmonent	Model	Parameter	Result
DXB	apec	kT (keV)	$0.106^{+0.004}_{-0.004}$
		Normalization (10^{-6})	$4.58^{+0.72}_{-0.71}$
	tbabs*apec	N_H (10^{20} cm^{-2})	1.39 (fixed)
		kT (keV)	$0.217^{+0.024}_{-0.022}$
		Normalization (10^{-7})	$7.60^{+2.42}_{-2.36}$
	tbabs*powerlaw	N_H (10^{20} cm^{-2})	1.39 (fixed)
		Photon Index	1.46 (fixed)
		Normalization (10^{-7})	$3.16^{+0.88}_{-0.85}$
Ins-line	Gaussian-MOS1	Center Energy (keV)	1.49 (fixed)
		Normalization (10^{-7})	$2.01^{+0.67}_{-0.67}$
	Gaussian-MOS2	Center Energy (keV)	1.49 (fixed)
		Normalization (10^{-8})	$6.65^{+7.08}_{-6.65}$
		Center Energy (keV)	1.75 (fixed)
		Normalization (10^{-9})	$8.03^{+43.77}_{-8.03}$
RSP	powerlaw-pn	Photon Index	$1.45^{+0.11}_{-0.10}$
		Normalization (10^{-4})	$4.12^{+0.37}_{-0.37}$
	powerlaw-MOS1	Photon Index	$1.13^{+0.14}_{-0.18}$
		Normalization (10^{-4})	$1.82^{+0.46}_{-0.46}$
	powerlaw-MOS2	Photon Index	$1.00^{+0.20}_{-0.27}$
		Normalization (10^{-4})	$1.28^{+0.46}_{-0.44}$
Fit statistic/degrees of freedom			309.80/294

Note. Normalizations are for 1 arcmin^{-2}. The areas of FOV for Obs391 are 273.68 (pn), 298.15 (MOS1) and 299.47 (MOS2) arcmin^{-2}, respectively. Very weak instrument emission lines are not listed in this table: Si K$_\alpha$ line (E ~ 1.75 keV) of MOS1 and Al K$_\alpha$ line (E ~ 1.49 keV) of pn.

---

[4] https://heasarc.gsfc.nasa.gov/lheasoft/

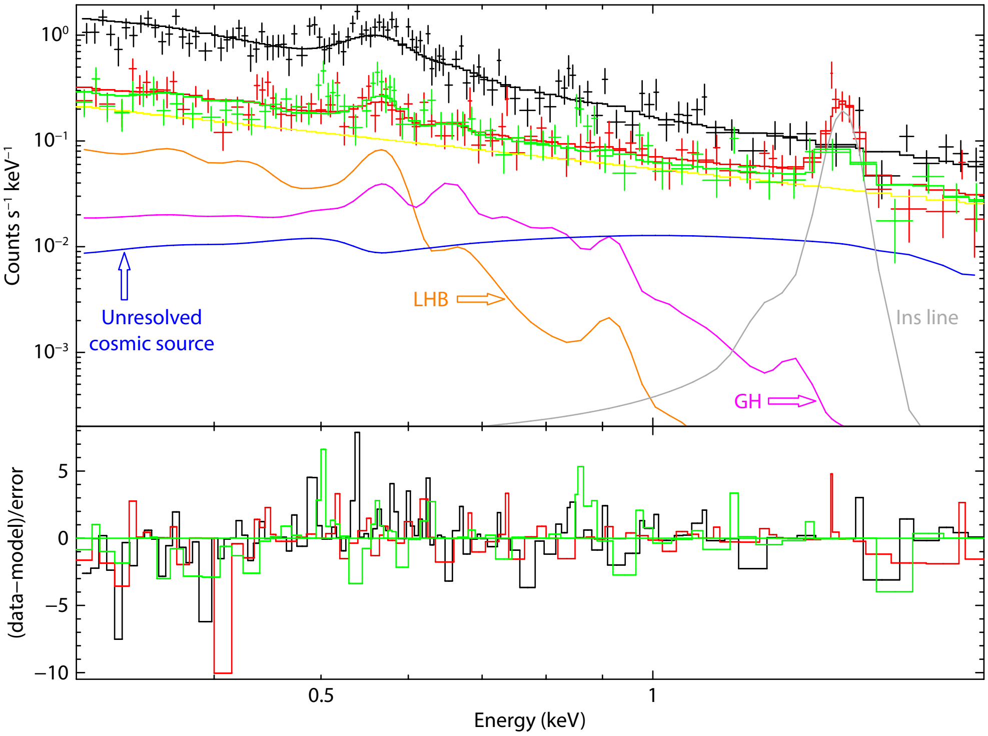

Figure 4. Clean spectrum of pn (black), MOS1 (red) and MOS2 (green) for Obs391 and the best-fitting models. Three components of DXB model are shown individually: the LHB (orange), the GH (purple), and the unresolved cosmic background (blue). The center energy of instrumental line (light grey) is fixed at 1.49 keV. The RSP is shown in yellow. The lower panel shows the variance between the data and total model (red). For clarity, only the model components of MOS1 (similar to MOS2 and pn) are shown.

Table 3. Best-fitting parameters for Obs2958 obtained by the two methods.

Conmonent	Model	Parameter	RASS method	Quiet method
DXB	apec	*kT* (keV)	$0.101^{+0.001}_{-0.001}$	0.106 (fixed)
		Normalization (10^{-6})	$4.50^{+2.08}_{-2.07}$	4.58 (fixed)
	tbabs*apec	N_H (10^{20} cm^{-2})	1.39 (fixed)	1.39 (fixed)
		kT (keV)	$0.249^{+0.009}_{-0.009}$	0.217 (fixed)
		Normalization (10^{-7})	$5.74^{+1.69}_{-1.25}$	7.60 (fixed)
	tbabs*powerlaw	N_H (10^{20} cm^{-2})	1.39 (fixed)	1.39 (fixed)
		Photon Index	1.46 (fixed)	1.46 (fixed)
		Normalization (10^{-7})	$3.33^{+0.63}_{-1.23}$	3.16 (fixed)
RSP	powerlaw-pn	Photon Index	0.60 (fixed)	0.60 (fixed)
		Normalization (10^{-6})	$1.87^{+16.53}_{-1.87}$	$3.96^{+8.81}_{-3.96}$
	powerlaw-MOS1	Photon Index	0.60 (fixed)	0.60 (fixed)
		Normalization (10^{-6})	$2.02^{+9.77}_{-2.02}$	$3.12^{+7.00}_{-3.12}$
	powerlaw-MOS2	Photon Index	$0.59^{+0.56}_{-0.86}$	$0.63^{+0.51}_{-0.87}$
		Normalization (10^{-5})	$5.09^{+6.75}_{-4.35}$	$5.77^{+5.70}_{-4.24}$
SWCX	Gaussian	Described in Table 4		
Fit statistic/degrees of freedom			383.67/382	382.36/380

Note. Normalizations are for 1 arcmin^{-2}. The areas of FOV for Obs2958 are 270.93 (pn), 196.93 (MOS1) and 69.90 (MOS2) arcmin^{-2}, respectively. The residual instrument lines do not exist.

are very close. The temperature of GH emission obtained by the RASS method is higher than that obtained by the Quiet method, while the normalization is the opposite. The photon index of unresolved cosmic background is fixed to 1.46, but the normalization obtained by the RASS method is slightly higher than that obtained by the Quiet method. Overall, the DXB intensity in 0.3–2.0 keV band obtained by the RASS method and Quiet method are 23.12 ± 0.54 and 25.96 ± 0.51 keV cm^{-2} s^{-1} sr^{-1}, respectively. Secondly, the photon index of RSP obtained by the two methods are almost identical, while the normalization obtained by the RASS method is only about half of that obtained by the Quiet method (MOS1 and pn).

Table 4 lists the best-fitting parameters of SWCX for Obs2958 obtained by the two methods, and Figure 6 shows the clean spectrum and best-fitting models. The dominant emission line obtained by both methods is the OVII line, and the compositions of emission lines obtained by the two methods are very similar, although their normalizations have some differences. The SWCX intensity in 0.3–2.0 keV band obtained by the RASS method and Quiet method are 13.45 ± 0.39 and 10.77 ± 0.40 keV cm^{-2} s^{-1} sr^{-1}, respectively. Overall, the magnetospheric SWCX intensity obtained by the RASS method is about 2.68 ± 0.56 keV cm^{-2} s^{-1} sr^{-1} higher than that obtained by the Quiet method, while the DXB intensity obtained by the RASS method is about 2.84 ± 0.74 keV cm^{-2} s^{-1} sr^{-1} lower than that obtained by the Quiet method. Since the differences between SWCX and DXB are highly consistent, the difference in magnetospheric SWCX emission obtained by the two methods can be generally attributed to the different estimate of DXB contribution.

4.2 Differences Between Two Methods at Different Energies

Figure 7 shows the intensities of DXB, RSP and magnetospheric SWCX for Obs2958 obtained by the two methods at different energies, as well as the differences between the two methods. It is evident that when the energy is less than 0.7 keV, the intensity of magnetospheric SWCX obtained by the RASS method is higher than that obtained by the Quiet method, while when the energy is greater than 0.7 keV, there is no significant difference. Firstly, the linear correlation coefficient of the difference between magnetospheric SWCX and DXB obtained by the two methods is close to −1, so the difference in magnetospheric SWCX can be fully attributed to the difference in DXB. Secondly, the biggest difference is in the 0.5–0.6 keV band, which is also the strongest band of SWCX emission. Thirdly, there is a relatively large difference in the 0.3–0.4 keV band, which may because only the R45 and R67 bands of RASS data were used in spectral fitting (the energy lower limit of all spectra was set to 0.3 keV). In addition, although the difference in RSP obtained by the two methods is relatively large, there is no significant impact on the contribution of DXB and SWCX.

4.3 Differences Between Two Methods under Different Solar Wind Conditions

Figure 8 shows the X-ray signals of Obs2958 under different solar wind conditions. Firstly, as shown in panel (b), the linear correlation coefficient between the SWCX intensity obtained by the two methods is close to 1. Therefore, the changes of SWCX emission over time obtained by the two methods are highly consistent. Secondly, as shown in panel (c), the difference in SWCX intensity obtained by the two methods fluctuates within 30%, and the linear correlation coefficient between the difference in SWCX emission and the SWCX intensity is −0.123. Therefore, the difference in SWCX emission obtained by the two methods is not related to the X-ray intensity. In general, the higher the solar wind proton flux, the stronger the SWCX intensity. The ratio of O^{7+} to O^{6+} characterizes the ionization state of solar wind ions, so the greater the ratio, the more high-valence ions which can generate SWCX emission. Therefore, to some extent, the difference between the two methods is not related to solar wind conditions. As shown in panels (a–b), the intensity of SWCX emission does almost always change with the solar wind, except for the last few hours, where the SWCX intensity increases while the solar wind weakens. As shown in panel (d), due to the fact that the energy

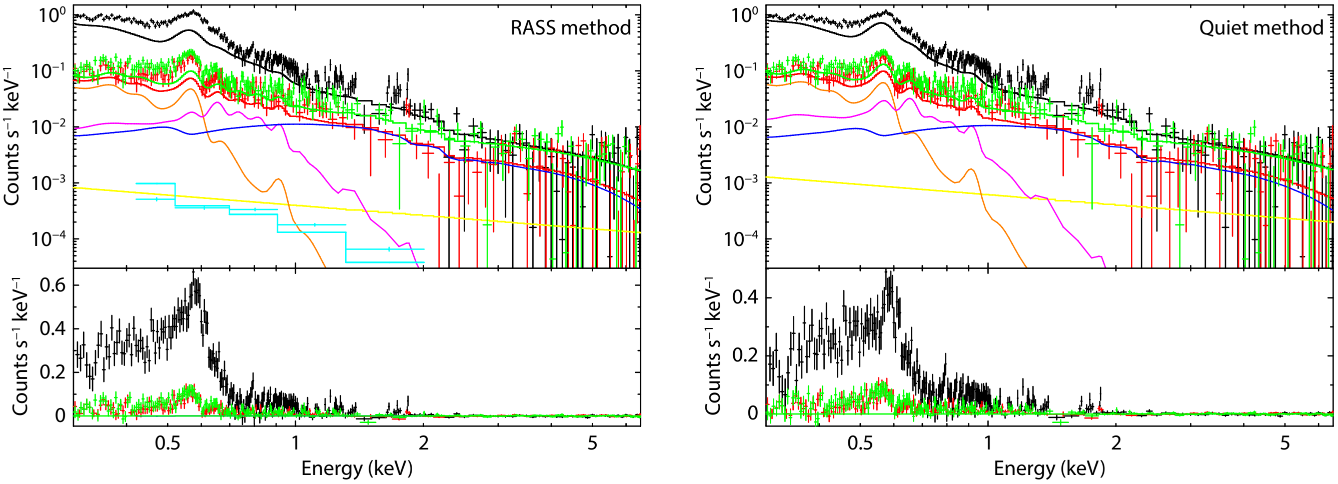

Figure 5. Clean spectrum of pn (black), MOS1 (red) and MOS2 (green) for Obs2958 and the best-fitting models of DXB and RSP obtained by RASS method (left) and Quiet method (right). RASS data is shown in light blue (left). Three components of DXB model are shown individually: LHB (orange), GH (purple), and unresolved cosmic background (blue). RSP model is shown in yellow. For clarity, only the model components of MOS1 (similar to MOS2 and pn) are shown. The lower panel shows the residual signals after removing DXB and RSP.

Table 4. Best-fitting parameters of SWCX for Obs2958 obtained by the two methods.

Line	Energy (keV)	Normalization (10^{-7})	
		RASS method	Quiet method
CVI	0.367	$4.314^{+4.369}_{-4.314}$	$2.720^{+1.395}_{-1.396}$
NVI	0.420	$0.809^{+0.834}_{-0.809}$	$0.772^{+0.822}_{-0.772}$
NVII	0.500	$1.623^{+0.435}_{-0.428}$	$1.514^{+0.393}_{-0.391}$
OVII	0.561	$4.341^{+1.413}_{-1.423}$	$2.888^{+0.267}_{-0.264}$
OVIII	0.653	$1.642^{+0.444}_{-0.492}$	$1.327^{+0.226}_{-0.224}$
FeXVII	0.73		$0.154^{+0.157}_{-0.154}$
FeXVII	0.82	$0.113^{+0.116}_{-0.113}$	$0.266^{+0.115}_{-0.165}$
FeXVIII	0.87		$0.017^{+0.200}_{-0.017}$
NeIX	0.92	$0.357^{+0.133}_{-0.239}$	$0.362^{+0.144}_{-0.222}$
FeXX	0.96	$0.125^{+0.188}_{-0.125}$	$0.135^{+0.183}_{-0.135}$
NeX	1.022	$0.190^{+0.115}_{-0.113}$	$0.220^{+0.108}_{-0.111}$
NeIX	1.10	$0.101^{+0.107}_{-0.079}$	$0.119^{+0.082}_{-0.082}$
NeX	1.22	$0.213^{+0.104}_{-0.090}$	$0.227^{+0.075}_{-0.074}$
MgXI	1.33	$0.106^{+0.098}_{-0.084}$	$0.121^{+0.072}_{-0.072}$
MgXI	1.60	$0.066^{+0.094}_{-0.066}$	$0.075^{+0.078}_{-0.075}$
AlXIII	1.73	$0.053^{+0.093}_{-0.053}$	$0.060^{+0.081}_{-0.060}$
SiXIII	1.85	$0.082^{+0.104}_{-0.082}$	$0.090^{+0.093}_{-0.090}$
SiXIV	2.00	$0.022^{+0.080}_{-0.022}$	$0.026^{+0.071}_{-0.026}$

Note. Normalizations are for 1 arcmin^{-2}. The areas of FOV for Obs2958 are 270.93 (pn), 196.93 (MOS1) and 69.90 (MOS2) arcmin^{-2}, respectively.

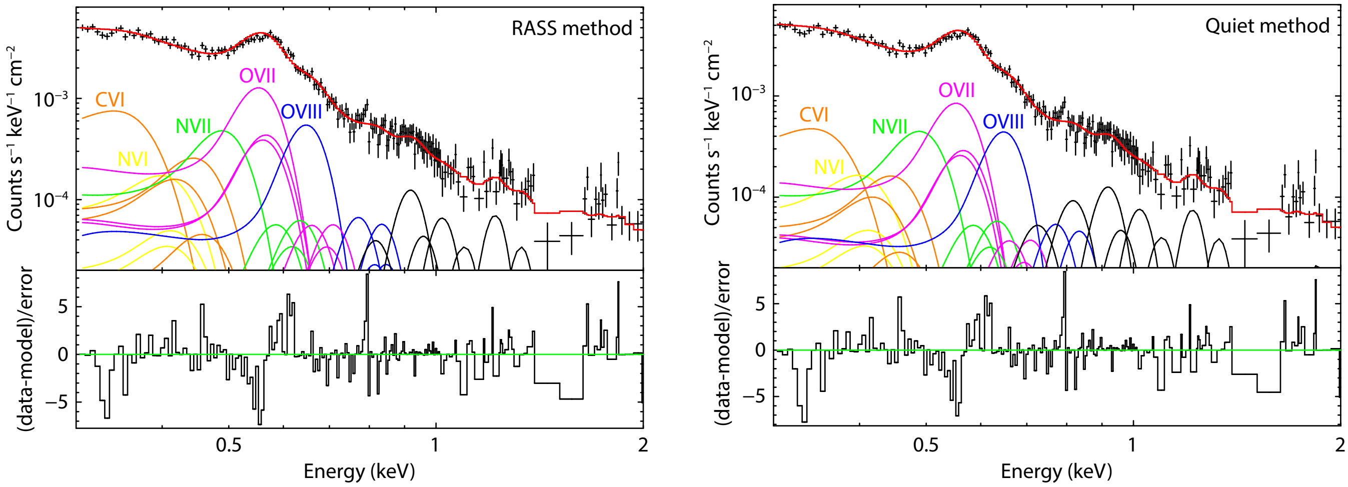

Figure 6. Clean spectrum of pn (similar to MOS) for Obs2958 and the best-fitting SWCX model obtained by RASS method (left) and Quiet method (right). The line emission from C, N and O are colored and that from heavier elements are black. The lower panel shows the variance between the total model (red curve) and the data.

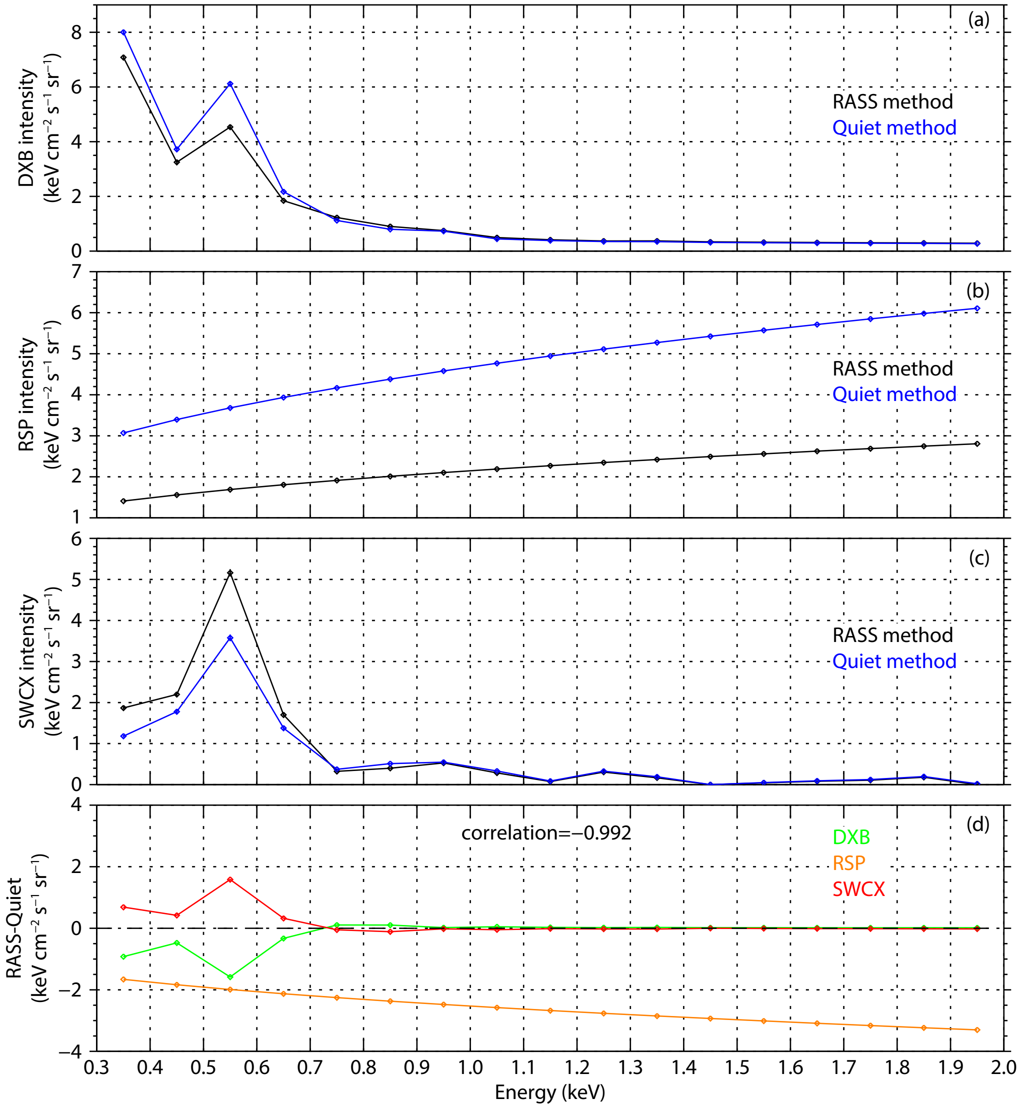

Figure 7. The X-ray intensities from different components of Obs2958’s pn camera (similar to MOS) obtained by the RASS method (black) and Quiet method (blue): (a) DXB, (b) RSP, and (c) magnetospheric SWCX. Panel (d) shows the difference between the X-ray intensities of different components obtained by the two methods: DXB (green), RSP (orange), and magnetospheric SWCX (red), as well as the linear correlation coefficient between the difference of DXB and magnetospheric SWCX (at the upper center of the panel). For comparison, the intensity of RSP is also folded through the instrumental effective areas.

bands unaffected by SWCX do not exhibit this phenomenon, it is speculated that there may be other factors that affect the intensity of SWCX emission, such as the time-varying LOS or neutral hydrogen density.

5. Discussions

The biggest difference between the RASS method and the Quiet method is the data used to fit the DXB. The RASS method uses the RASS data obtained during the 6-month period approaching the solar maximum (1990–1991), which consists of the CDXB and heliospheric SWCX emission. The Quiet method uses the data observed under weaker solar wind conditions, which consists of the CDXB, heliospheric SWCX emission, weaker magnetospheric SWCX emission and possible RSP. Firstly, the CDXB does not change over time, so it does not change between different instruments and observations. Secondly, the heliospheric SWCX emission changes with the solar cycle, so this work selected the observation that occurred in the solar maximum year (2002), similar to the RASS data (1990–1991), as the quiet observation. However, there are differences in the strength of solar activity among different solar cycles. Thirdly, in order to eliminate the impact of weaker magnetospheric SWCX emission, this work selected the observation with the LOS pointing towards the night side magnetosphere, as the quiet observation. However, the SWCX emission on the flank of magnetosheath still exists, even if it is very weak. Fourthly, soft proton flares changes over time, so the RSP observed during the quiet observation and the scientific observation must be different. In summary, although very strict conditions have been adopted in this work, resulting in extremely rare quiet observations that meet the requirements, there are still inevitable differences between the data used by the two methods, which is also the reason for some differences in the fitting results of the two methods.

For the Quiet method, since soft proton flares are inevitably differ-

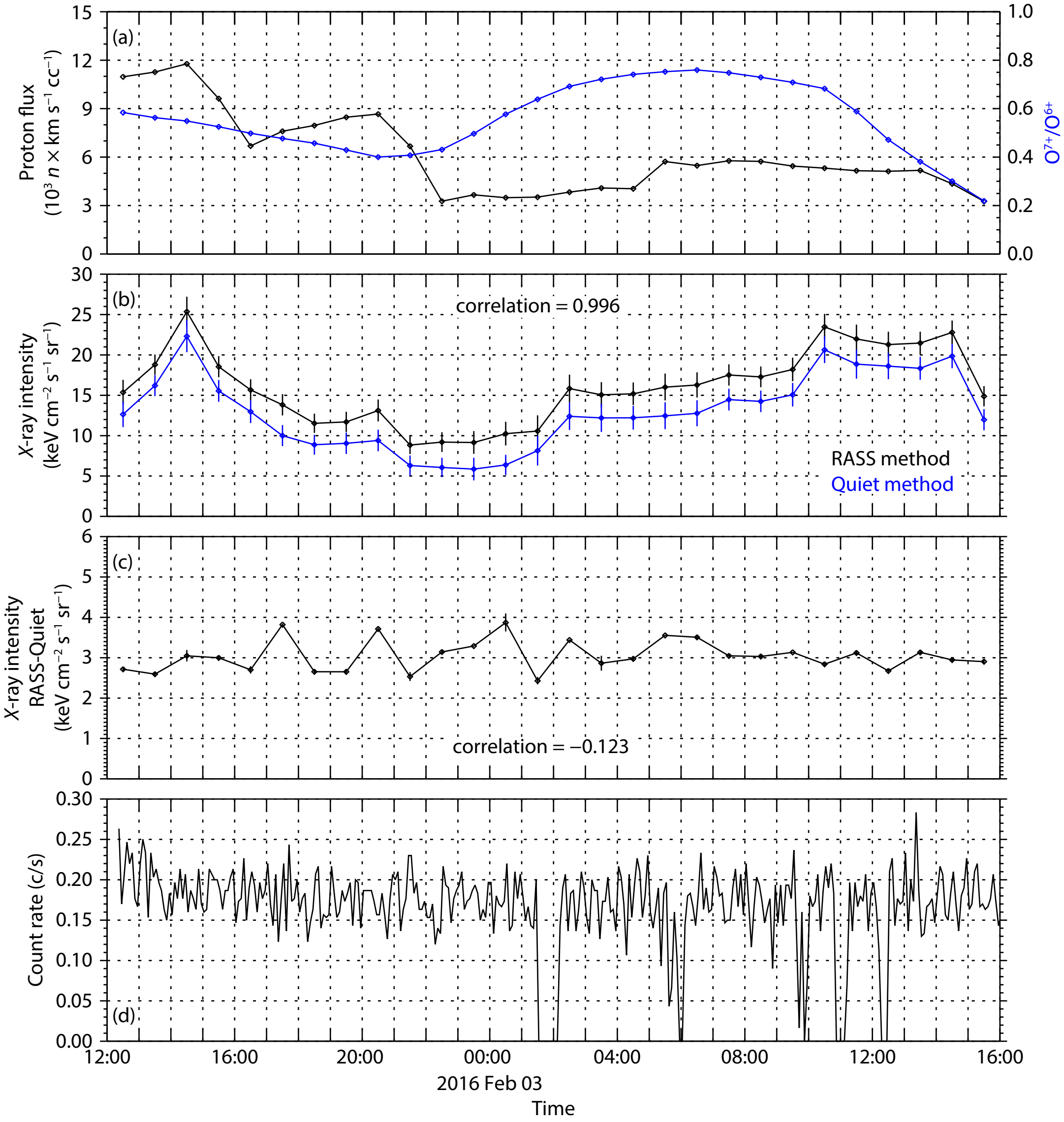

Figure 8. X-ray signals of Obs2958 under different solar wind conditions. (a) solar wind proton density (black) and the ratio of O^{7+} to O^{6+} (blue). (b) Magnetospheric SWCX emission intensity of pn camera (similar to MOS) obtained by the RASS method (black) and Quiet method (blue), as well as the linear correlation coefficient between them (at the upper center of the panel). (c) The difference between the X-ray intensity obtained by the two methods, as well as the linear correlation coefficient between it and the SWCX intensity (at the bottom center of the panel). (d) The count rate of pn camera (similar to MOS) in the energy range of 2.5–5.0 keV.

ent between different observations, even if the quiet observation data is poor, as long as the fitting is adequate, it will not have a significant impact on the final results. Due to the scarcity of quiet observations that meet general requirements, this has to some extent expanded the applicability of the Quiet method. For the RASS method, since all the RASS data are obtained during the solar maximum, it may be more suitable for scientific observations that occur during the solar maximum. However, eROSITA (Predehl et al., 2021) has begun a new survey of the entire sky on December 13, 2019. It is expected that by the end of 2023, eight complete scans of the entire sky will be conducted, and its sensitivity of the final eROSITA All-Sky Survey in the soft X-ray band (0.2–2.3 keV) will be about 25 times higher than that of RASS. Although the data collection of eROSITA ended in February 2022, it has accumulated some data observed during the solar minimum, which can compensate for some limitations of the RASS method. Moreover, if eROSITA can restart the survey, it will be a huge piece of good news for SMILE which will be launched in 2025.

6. Conclusion

This paper compares the magnetospheric SWCX emission obtained by the two methods in an XMM-Newton observation, during which the solar wind changed dramatically. The two methods differ in the data used to fit the DXB parameters in spectral analysis. The RASS method adds data from RASS to constrain the DXB parameters. The Quiet method uses a quiet observation to directly fit the DXB parameters. Results show that the spectral compositions of magnetospheric SWCX emission obtained by the two methods are very similar, and the changes in intensity over time are highly consistent, although the intensity obtained by the RASS method is about 2.68 ± 0.56 keV cm^{-2} s^{-1} sr^{-1} higher than that obtained by the

Quiet method. Since the DXB intensity obtained by the RASS method is about 2.84 ± 0.74 keV cm^{-2} s^{-1} sr^{-1} lower than that obtained by the Quiet method, and the linear correlation coefficient between the difference of SWCX and DXB obtained by the two methods in different energy band is close to −1, the differences in magnetospheric SWCX can be fully attributed to the differences in the fitted DXB. The difference between the two methods is most significant when the energy is less than 0.7 keV, which is also the main energy band of SWCX emission. In addition, the difference between the two methods is not related to the SWCX intensity and, to some extent, to solar wind conditions, because SWCX intensity typically varies with the solar wind. In summary, both methods are robust and reliable, and should be considered based on the best available options.

Acknowledgments

This work was supported by NNSFC grants 42322408, 42188101 and 42074202; the Strategic Pioneer Program on Space Science, CAS Grant nos. XDA15350201, and in part by the Research Fund from the Chinese Academy of Sciences and the Specialized Research Fund for State Key Laboratories of China. Tianran Sun is also supported by the Young Elite Scientists Sponsorship Program (CAST-Y20 2045). Jennifer. A. Carter is supported by Royal Society grant DHF\R1\211068.

Appendix A

Supplementary Materials

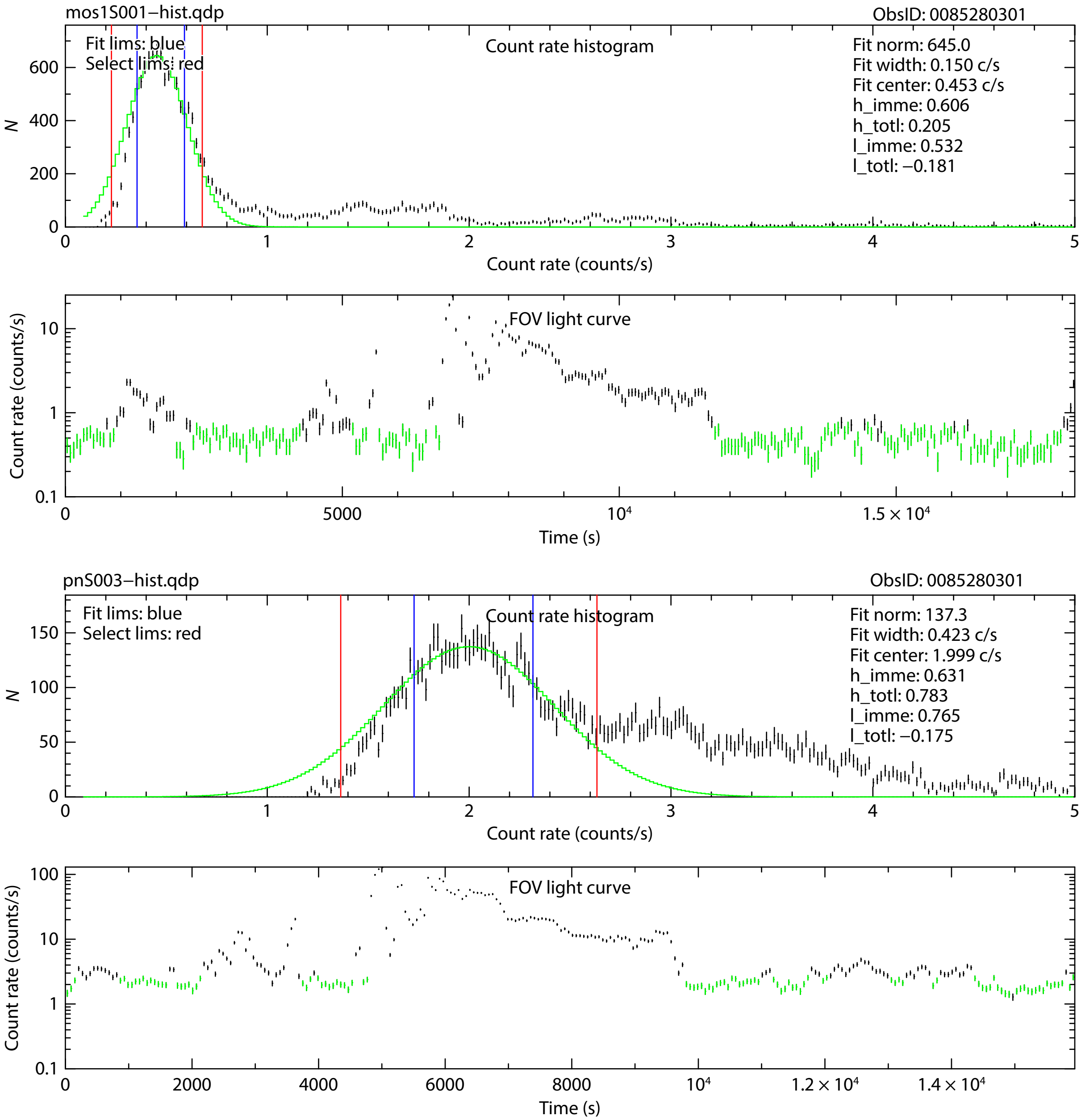

Figure S1. Temporal filtering results of MOS1 (similar to MOS2) and pn for Obs391. In the Count Rate Histogram panel, the blue vertical lines display the range of Gaussian fitting, the green curve displays Gaussian fitting, and the red vertical lines display the upper and lower limits of filtered data. In the FOV Light Curve panel, green dots represent accepted data, and black dots represent data excluded by the filtering algorithm.

References

Asakura, K., Matsumoto, H., Okazaki, K., Yoneyama, T., Noda, H., Hayashida, K., Tsunemi, H., Nakajima, H., Katsuda, S., … Ezoe, Y. (2021). Suzaku detection of solar wind charge exchange emission from a variety of highly ionized ions in an interplanetary coronal mass ejection. *Publ. Astron. Soc. Jpn.*, *73*(3), 504–518. https://doi.org/10.1093/pasj/psab015

Bhardwaj, A., Elsner, R. F., Gladstone, G. R., Cravens, T. E., Lisse, C. M., Dennerl, K., Branduardi-Raymont, G., Wargelin, B. J., Waite, J. H. Jr., … Kharchenko, V. (2007). X-rays from solar system objects. *Planet. Space Sci.*, *55*(9), 1135–1189. https://doi.org/10.1016/j.pss.2006.11.009

Bodewits, D., Christian, D. J., Torney, M., Dryer, M., Lisse, C. M., Dennerl, K., Zurbuchen, T. H., Wolk, S. J., Tielens, A. G. G. M., and Hoekstra, R. (2007). Spectral analysis of the *Chandra* comet survey. *A&A*, *469*(3), 1183–1195. https://doi.org/10.1051/0004-6361:20077410

Branduardi-Raymont, G., Elsner, R. F., Gladstone, G. R., Ramsay, G., Rodriguez, P., Soria, R., and Waite, J. H. (2004). First observation of Jupiter by *XMM-Newton*. *A&A*, *424*(1), 331–337. https://doi.org/10.1051/0004-6361:20041149

Branduardi-Raymont, G., Sembay, S. F., Eastwood, J. P., Sibeck, D. G., Abbey, T. A., Brown, P., Carter, J. A., Carr, C. M., Forsyth, C., … Yeoman, T. K. (2012). AXIOM: advanced X-ray imaging of the magnetosphere. *Exp. Astron.*, *33*(2), 403–443. https://doi.org/10.1007/s10686-011-9239-0

Branduardi-Raymont, G., Wang, C., Escoubet, C. P., Adamovic, M., Agnolon, D., Berthomier, M., Carter, J. A., Chen, W., Colangeli, L., … Zhu, Z. (2018). Smile definition study report (red book). SMILE definition study report. *European Space Agency*, *ESA/SCI*, 1, 1-86. https://doi.org/10.5270/esa.smile.definition_study_report-2018-12

Carter, J. A., and Sembay, S. (2008). Identifying XMM-Newton observations affected by solar wind charge exchange Part I. *A&A*, *489*(2), 837–848. https://doi.org/10.1051/0004-6361:200809997

Carter, J. A., Sembay, S., and Read, A. M. (2010). A high charge state coronal mass ejection seen through solar wind charge exchange emission as detected by *XMM–Newton*. *Mon. Not. R. Astron. Soc.*, *402*(2), 867–878. https://doi.org/10.1111/j.1365-2966.2009.15985.x

Carter, J. A., Sembay, S., and Read, A. M. (2011). Identifying XMM-*Newton* observations affected by solar wind charge exchange – Part II. *A&A*, *527*, A115. https://doi.org/10.1051/0004-6361/201015817

Carter, J. A., Sembay, S., and Read, A. M. (2012). Exospheric solar wind charge exchange as seen by XMM-Newton. *Astron. Nachr.*, *333*(4), 313–318. https://doi.org/10.1002/asna.201211661

Chao, J. K., Wu, D. J., Lin, C. H., Yang, Y. H., Wang, X. Y., Kesse, M., Shen, S. H., and Lepping, R. P. (2002). Models for the size and shape of the earth's magnetopause and bow shock. *COSPAR Colloq. Ser.*, *12*, 127–135. https://doi.org/10.1016/S0964-2749(02)80212-8

Collier, M. R., Porter, F. S., Sibeck, D. G., Carter, J. A., Chiao, M. P., Chornay, D., Cravens, T., Galeazzi, M., Keller, J. W., … Thomas, N. (2012). Prototyping a global soft X-ray imaging instrument for heliophysics, planetary science, and astrophysics science. *Astron. Nachr.*, *333*(4), 378–382. https://doi.org/10.1002/asna.201211662

Collier, M. R., Snowden, S. L., Sarantos, M., Benna, M., Carter, J. A., Cravens, T. E., Farrell, W. M., Fatemi, S., Hills, H. K., … Walsh, B. M. (2014). On lunar exospheric column densities and solar wind access beyond the terminator from ROSAT soft X-ray observations of solar wind charge exchange. *J. Geophys. Res.: Planets*, *119*(7), 1459–1478. https://doi.org/10.1002/2014JE004628

Cox, D. P. (1998). Modeling the local bubble. In D. Breitschwerdt, et al. (Eds.), *The Local Bubble and Beyond* (pp. 121-131). Berlin, Heidelberg: Springer. https://doi.org/10.1007/BFb0104706

Cravens, T. E. (1997). Comet Hyakutake X-ray source: Charge transfer of solar wind heavy ions. *Geophys. Res. Lett.*, *24*(1), 105–108. https://doi.org/10.1029/96GL03780

Cravens, T. E., Robertson, I. P., and Snowden, S. L. (2001). Temporal variations of geocoronal and heliospheric X-ray emission associated with the solar wind interaction with neutrals. *J. Geophys. Res.: Space Phys.*, *106*(A11), 24883–24892. https://doi.org/10.1029/2000JA000461

Dennerl, K., Lisse, C. M., Bhardwaj, A., Burwitz, V., Englhauser, J., Gunell, H., Holmström, M., Jansen, F., Kharchenko, V., and Rodríguez-Pascual, P. M. (2006). First observation of Mars with XMM-Newton: high resolution X-ray spectroscopy with RGS. *A&A*, *451*(2), 709–722. https://doi.org/10.1051/0004-6361:20054253

Dennerl, K. (2008). X-rays from Venus observed with Chandra. *Planet. Space Sci.*, *56*(10), 1414–1423. https://doi.org/10.1016/j.pss.2008.03.008

Ezoe, Y., Ebisawa, K., Yamasaki, N. Y., Mitsuda, K., Yoshitake, H., Terada, N., Miyoshi, Y., and Fujimoto, R. (2010). Time variability of the geocoronal solar-wind charge exchange in the direction of the celestial equator. *Publ. Astron. Soc. Jpn.*, *62*(4), 981–986. https://doi.org/10.1093/pasj/62.4.981

Ezoe, Y., Miyoshi, Y., Yoshitake, H., Mitsuda, K., Terada, N., Oishi, S., and Ohashi, T. (2011). Enhancement of terrestrial diffuse X-ray emission associated with coronal mass ejection and geomagnetic storm. *Publ. Astron. Soc. Jpn.*, *63*(sp3), S691–S704. https://doi.org/10.1093/pasj/63.sp3.S691

Fujimoto, R., Mitsuda, K., McCammon, D., Takei, Y., Bauer, M., Ishisaki, Y., Porter, F. S., Yamaguchi, H., Hayashida, K., and Yamasaki, N. Y. (2007). Evidence for solar-wind charge-exchange X-ray emission from the Earth's magnetosheath. *Prog. Theor. Phys. Suppl.*, *169*, 71–74. https://doi.org/10.1143/PTPS.169.71

Galeazzi, M., Collier, M. R., Cravens, T., Koutroumpa, D., Kuntz, K. D., Lepri, S., McCammon, D., Porter, F. S., Prasai, K.,…Uprety, Y. (2012). Solar wind charge exchange and local hot bubble X-ray emission with the DXL sounding rocket experiment. *Astron. Nachr.*, *333*(4), 383–387. https://doi.org/10.1002/asna.201211665

Galeazzi, M., Chiao, M., Collier, M. R., Cravens, T., Koutroumpa, D., Kuntz, K. D., Lallement, R., Lepri, S. T., McCammon, D., … Walsh, B. M. (2014). The origin of the local 1/4-keV X-ray flux in both charge exchange and a hot bubble. *Nature*, *512*(7513), 171–173. https://doi.org/10.1038/nature13525

Henley, D. B., and Shelton, R. L. (2008). Comparing *Suzaku* and *XMM-Newton* observations of the soft X-ray background: Evidence for solar wind charge exchange emission. *Astrophys. J.*, *676*(1), 335–350. https://doi.org/10.1086/528924

Ishi, D., Ishikawa, K., Numazawa, M., Miyoshi, Y., Terada, N., Mitsuda, K., Ohashi, T., and Ezoe, Y. (2019). Suzaku detection of enigmatic geocoronal solar wind charge exchange event associated with coronal mass ejection. *Publ. Astron. Soc. Jpn.*, *71*(1), 23. https://doi.org/10.1093/pasj/psy142

Ishikawa, K., Ezoe, Y., Miyoshi, Y., Terada, N., Mitsuda, K., and Ohashi, T. (2013). Suzaku observation of strong solar-wind charge-exchange emission from the terrestrial exosphere during a geomagnetic storm. *Publ. Astron. Soc. Jpn.*, *65*(3), 63. https://doi.org/10.1093/pasj/65.3.63

Koutroumpa, D., Lallement, R., Kharchenko, V., Dalgarno, A., Pepino, R., Izmodenov, V., and Quémerais, E. (2006). Charge-transfer induced EUV and soft X-ray emissions in the heliosphere. *A&A*, *460*(1), 289–300. https://doi.org/10.1051/0004-6361:20065250

Koutroumpa, D., Acero, F., Lallement, R., Ballet, J., and Kharchenko, V. (2007). OVII and OVIII line emission in the diffuse soft X-ray background: heliospheric and galactic contributions. *A&A*, *475*(3), 901–914. https://doi.org/10.1051/0004-6361:20078271

Koutroumpa, D., Lallement, R., Raymond, J. C., and Kharchenko, V. (2009a). The solar wind charge-transfer X-ray emission in the 1/4 keV energy range: Inferences on local bubble hot gas at low *Z. Astrophys. J.*, *696*(2), 1517–1525. https://doi.org/10.1088/0004-637x/696/2/1517

Koutroumpa, D., Collier, M. R., Kuntz, K. D., Lallement, R., and Snowden, S. L. (2009b). Solar wind charge exchange emission from the helium focusing cone: Model to data comparison. *Astrophys. J.*, *697*(2), 1214–1225. https://doi.org/10.1088/0004-637x/697/2/1214

Koutroumpa, D., Lallement, R., and Kharchenko, V. (2009c). The spectrum of the solar wind charge exchange emission: Contribution to the soft X-ray background. *AIP Conf. Proc.*, *1156*(1), 62–73. https://doi.org/10.1063/1.3211835

Kuntz, K. D., and Snowden, S. L. (2000). Deconstructing the spectrum of the soft X-ray background. *Astrophys. J.*, *543*(1), 195–215. https://doi.org/10.1086/317071

Kuntz, K. D., and Snowden, S. L. (2008a). The X-ray-emitting components toward ℓ= 111°: The local hot bubble and beyond. *Astrophys. J.*, *674*(1), 209–219. https://doi.org/10.1086/524719

Kuntz, K. D., and Snowden, S. L. (2008b). The EPIC-MOS particle-induced background spectra. *A&A*, *478*(2), 575–596. https://doi.org/10.1051/0004-6361:20077912

Kuntz, K. D., Collado-Vega, Y. M., Collier, M. R., Connor, H. K., Cravens, T. E., Koutroumpa, D., Porter, F. S., Robertson, I. P., Sibeck, D. G., … Walsh, B. M. (2015). The solar wind charge-exchange production factor for hydrogen. *Astrophys. J.*, *808*(2), 143. https://doi.org/10.1088/0004-637x/808/2/143

Kuntz, K. D. (2019). Solar wind charge exchange: an astrophysical nuisance. *Astron. Astrophys. Rev.*, *27*, 1. https://doi.org/10.1007/s00159-018-0114-0

Lallement, R. (2004). The heliospheric soft X-ray emission pattern during the ROAST survey: Inferences on local bubble hot gas. *A&A*, *418*(1), 143–150. https://doi.org/10.1051/0004-6361:20040059

Lisse, C. M., Dennerl, K., Englhauser, J., Harden, M., Marshall, F. E., Mumma, M. J., Petre, R., Pye, J. P., Ricketts, M. J.,… West, R. G. (1996). Discovery of X-ray and extreme ultraviolet emission from comet C/hyakutake 1996 B2. *Science*, *274*(5285), 205-209. https://doi.org/10.1126/science.274.5285.205

McCammon, D., and Sanders, W. T. (1990). The soft X-ray background and its origins. *Annu. Rev. Astron. Astrophys.*, *28*(1), 657–688. https://doi.org/10.1146/annurev.aa.28.090190.003301

Mushotzky, R. F., Cowie, L. L., Barger, A. J., and Arnaud, K. A. (2000). Resolving the extragalactic hard X-ray background. *Nature*, *404*(6777), 459–464. https://doi.org/10.1038/35006564

Predehl, P., Andritschke, R., Arefiev, V., Babyshkin, V., Batanov, O., Becker, W., Böhringer, H., Bogomolov, A., Boller, T., …Yaroshenko, V. (2021). The eROSITA X-ray telescope on SRG. *A&A*, *647*, A1. https://doi.org/10.1051/0004-6361/202039313

Qu, Z. J., Koutroumpa, D., Bregman, J. N., Kuntz, K. D., and Kaaret, P. (2022). The solar cycle temporal variation of the solar wind charge exchange X-ray lines. *Astrophys. J.*, *930*(1), 21. https://doi.org/10.3847/1538-4357/ac6349

Robertson, I. P., Kuntz, K. D., Collier, M. R., Cravens, T. E., and Snowden, S. L. (2009). The heliospheric contribution to the soft X-ray background emission. *AIP Conf. Proc.*, *1156*(1), 52–61. https://doi.org/10.1063/1.3211834

Shue, J. H., Chao, J. K., Fu, H. C., Russell, C. T., Song, P., Khurana, K. K., and Singer, H. J. (1997). A new functional form to study the solar wind control of the magnetopause size and shape. *J. Geophys. Res.: Space Phys.*, *102*(A5), 9497–9511. https://doi.org/10.1029/97JA00196

Sibeck, D. G., Allen, R., Aryan, H., Bodewits, D., Brandt, P., Branduardi-Raymont, G., Brown, G., Carter, J. A., Collado-Vega, Y. M., … Wing, S. (2018). Imaging plasma density structures in the soft X-rays generated by solar wind charge exchange with neutrals. *Space Sci. Rev.*, *214*(4), 79–124. https://doi.org/10.1007/s11214-018-0504-7

Slavin, J. D., Wargelin, B. J., and Koutroumpa, D. (2013). Solar wind charge exchange emission in the Chandra deep field north. *Astrophys. J.*, *779*(1), 13. https://doi.org/10.1088/0004-637X/779/1/13

Smith, R. K., Brickhouse, N. S., Liedahl, D. A., and Raymond, J. C. (2001). Collisional plasma models with APEC/APED: Emission-line diagnostics of hydrogen-like and helium-like ions. *Astrophys. J.*, *556*(2), L91–L95. https://doi.org/10.1086/322992

Snowden, S. L., McCammon, D., Burrows, D. N., and Mendenhall, J. A. (1994). Analysis procedures for ROSAT XRT/PSPC observations of extended objects and the diffuse background. *Astrophys. J.*, *424*, 714–728. https://doi.org/10.1086/173925

Snowden, S. L., Freyberg, M. J., Plucinsky, P. P., Schmitt, J. H. M. M., Trümper, J., Voges, W., Edgar, R. J., McCammon, D., and Sanders, W. T. (1995). First maps of the soft X-ray diffuse background from the ROSAT XRT/PSPC all-sky survey. *Astrophys. J.*, *454*, 643–653. https://doi.org/10.1086/176517

Snowden, S. L., Egger, R., Freyberg, M. J., McCammon, D., Plucinsky, P. P., Sanders, W. T., Schmitt, J. H. M. M., Trümper, J., and Voges, W. (1997). *ROSAT* survey diffuse X-ray background maps II. *Astrophys. J.*, *485*(1), 125–135. https://doi.org/10.1086/304399

Snowden, S. L., Collier, M. R., and Kuntz, K. D. (2004). *XMM-Newton* observation of solar wind charge exchange emission. *Astrophys. J.*, *610*(2), 1182–1190. https://doi.org/10.1086/421841

Snowden, S. L., Chiao, M., Collier, M. R., Porter, F. S., Thomas, N. E., Cravens, T., Robertson, I. P., Galeazzi, M., Uprety, Y., … Walsh, B. M. (2014). Pressure equilibrium between the local interstellar clouds and the local hot bubble. *Astrophys. J.*, *791*(1), L14. https://doi.org/10.1088/2041-8205/791/1/l14

Uprety, Y., Chiao, M., Collier, M. R., Cravens, T., Galeazzi, M., Koutroumpa, D., Kuntz, K. D., Lallement, R., Lepri, S. T., … Walsh, B. M. (2016). Solar wind charge exchange contribution to the *ROSAT* all sky survey maps. *Astrophys. J.*, *829*(2), 83. https://doi.org/10.3847/0004-637x/829/2/83

Walsh, B. M., Kuntz, K. D., Collier, M. R., Sibeck, D. G., Snowden, S. L., and Thomas, N. E. (2014). Energetic particle impact on X-ray imaging with XMM-Newton. *Space Wea.*, *12*(6), 387–394. https://doi.org/10.1002/2014SW001046

Walsh, B. M., Collier, M. R., Kuntz, K. D., Porter, F. S., Sibeck, D. G., Snowden, S. L., Carter, J. A., Collado-Vega, Y., Connor, H. K.,… Thomas, N. E. (2016). Wide field-of-view soft X-ray imaging for solar wind-magnetosphere interactions. *J. Geophys. Res.: Space Phys.*, *121*(4), 3353–3361. https://doi.org/10.1002/2016JA022348

Wang, C., and Branduardi-Raymont, G. (2020). Update on the ESA-CAS joint solar wind magnetosphere ionosphere link explorer (SMILE) mission. *Chin. J. Space Sci.*, *40*(5), 700–703. https://doi.org/10.11728/cjss2020.05.700

Wargelin, B. J., Markevitch, M., Juda, M., Kharchenko, V., Edgar, R., and Dalgarno, A. (2004). *Chandra* observations of the “dark” moon and geocoronal solar wind charge transfer. *Astrophys. J.*, *607*(1), 596–610. https://doi.org/10.1086/383410

Wargelin, B. J., Kornbleuth, M., Martin, P. L., and Juda, M. (2014). Observation and modeling of geocoronal charge exchange X-ray emission during solar wind gusts. *Astrophys. J.*, *796*(1), 28. https://doi.org/10.1088/0004-637x/796/1/28

Wilms, J., Allen, A., and McCray, R. (2000). On the absorption of X-rays in the interstellar medium. *Astrophys. J.*, *542*(2), 914–924. https://doi.org/10.1086/317016

Zhang, Y. J., Sun, T. R., Wang, C., Ji, L., Carter, J. A., Sembay, S., Koutroumpa, D., Liu, Y. D., Liang, G. Y., … Zhao, X. W. (2022). Solar wind charge exchange soft X-ray emissions in the magnetosphere during an interplanetary coronal mass ejection compared to its driven sheath. *Astrophys. J. Lett.*, *932*(1), L1. https://doi.org/10.3847/2041-8213/ac7521